Journal of Materials Chemistry A

PAPER

View Article Online
View Journal

Cite this: DOI: 10.1039/c6ta09220a

Electrochemical properties and structural evolution of O3-type layered sodium mixed transition metal oxides with trivalent nickel†

Plousia Vassilaras,[a] Deok-Hwang Kwon,[b] Stephen T. Dacek,[a] Tan Shi,[b] Dong-Hwa Seo,[b] Gerbrand Ceder[abc] and Jae Chul Kim*[c]

Received 24th October 2016
Accepted 29th January 2017

DOI: 10.1039/c6ta09220a

rsc.li/materials-a

The electrochemical properties of $NaNi_{0.5}Co_{0.5}O_2$ and $NaNi_{0.5}Fe_{0.5}O_2$ and their structural transitions as a function of Na extraction associated with redox reactions are investigated in this work. Synthesized in the O3-type layered structure, both materials show reasonable electrochemical activities at room temperature, delivering approximately 0.5 Na per formula unit at C/10 discharge. More Na can be reversibly cycled in $NaNi_{0.5}Co_{0.5}O_2$ at elevated temperature and/or in an extended voltage window, while $NaNi_{0.5}Fe_{0.5}O_2$ shows significant capacity fading at a high voltage cutoff which is likely due to Fe^{4+} migration. *In situ* X-ray diffraction shows that the structural changes in the two materials upon desodiation are very different. $NaNi_{0.5}Co_{0.5}O_2$ goes through many different two-phase reactions including three different O3-type and three different P3-type structures during cycling, producing a voltage profile with multiple plateau-like features. In contrast, $NaNi_{0.5}Fe_{0.5}O_2$ has a smooth voltage profile and shows the typical O3–P3 phase transition without lattice distortion seen in other materials. This different structural evolution upon desodiation and re-sodiation can be explained by the electronic structure of the mixed transition metals and how it perturbs the ordering between Na ions differently.

1. Introduction

Recent progress in the development of high-performance cathodes for rechargeable alkali-ion batteries has stimulated substantial research interest in exploring new materials and their synthesis routes.[1–8] Many oxides, sulfides, and polyanionic compounds can host Li, Na, or K and provide one-, two-, or three-dimensional diffusion pathways for the alkali ions to exit and enter the materials without disrupting the overall structure.[9–17] In the process, charge neutrality is maintained by oxidation and reduction of transition metals (M) and/or anions in the compound.[18] Simple dioxides with an ordered rock-salt structure can store a large amount of charge per unit mass and volume due to the low mass to negative charge ratio and the close-packed structure, although oxygen gas may evolve if overcharged.[19] Polyanionic compounds such as borates, phosphates, and sulfates, and their carbonated and fluorinated versions tend to have lower specific energy and energy density due to a larger formula weight.[20–25] Yet, these materials can have high redox potential and suppress the oxygen loss by the strong covalent bonding between anions and the main group metals, leading to a superior charged state stability.[12]

Ordered alkali transition metal oxides are distinguished by the arrangement of the oxygen ions. The hexagonal layers of oxygen ions can be stacked in several different ways, generating prismatic (P) or octahedral (O) sites for alkali ions and an octahedral site for transition metals.[26] For instance, in a P2-type stacking, alkali ions occupy the prismatic site provided by the sheets of edge-sharing MO_6 octahedra with a repeat unit of two layers (the ABBA stacking) while in an O3-type stacking, alkali ions are located in octahedral sites between the MO_6 layers with a stacking period of three (the ABCABC stacking).[26] The O3-type structures are frequently found in Li and Na compounds. In contrast, the P2 stacking is mostly observed in Na and K compounds as the large size of the prismatic site can accommodate large alkali ions. The P2 structure is only obtained when the Na and K contents are less than one per formula unit.[27,28]

As a cathode material for Na-ion batteries, P2-type layered Na transition metal oxides (P2-$NaMO_2$) show superior specific power originating from facile Na migration through the face-sharing prismatic sites.[29] Yet, their capacity is often limited due to the Na-deficiency in their structure, especially when combined with non-Na-containing anodes.[30] O3-type Na compounds (O3-$NaMO_2$) have attracted particular attention because of their potential for substantial and reversible Na intercalation, as

[a]Department of Materials Science and Engineering, Massachusetts Institute of Technology, Cambridge, Massachusetts 02139, USA

[b]Department of Materials Science and Engineering, University of California, Berkeley, California 94720, USA

[c]Materials Sciences Division, Lawrence Berkeley National Laboratory, Berkeley, California 94720, USA. E-mail: jckim@lbl.gov

† Electronic supplementary information (ESI) available. See DOI: 10.1039/c6ta09220a

demonstrated in O3-type Li transition metal oxides.[31] The electrochemical performance of these oxides has been investigated for a wide variety of compositions containing a single transition metal (M: Ti, V, Cr, Mn, Fe, Co, Ni)[32–40] or multiple transition metals in binary (M: $Mn_{0.5}Ni_{0.5}$, $Mn_{0.5}Fe_{0.5}$, $Co_{0.5}Fe_{0.5}$),[41–43] ternary (M: $Mn_{0.33}Co_{0.33}Ni_{0.33}$, $Mn_{0.33}Fe_{0.33}Ni_{0.33}$, $Fe_{0.33}Co_{0.33}Ni_{0.33}$),[44–46] and quaternary (M: $Mn_{0.25}Fe_{0.25}Co_{0.25}Ni_{0.25}$) mixtures.[47]

Previously, we revisited $NaNiO_2$ as a Na intercalation material.[37] This compound has the same layer stacking sequence as the O3-type material but exhibits monoclinicity (*i.e.*, an O′3 structure) due to the Jahn-Teller distortion of the trivalent Ni.[37] This effect can be suppressed by substituting a portion of Ni with other transition metals, such as Mn, Fe, and/or Co in the fully sodiated state.[47–49] In this paper, we investigate the effect of transition metal substitution on the O3-type layered rock-salt structure in $Na_{1-x}Ni_{0.5}M_{0.5}O_2$ ($x > 0$) with trivalent Ni, and their electrochemical properties as positive electrode materials for Na-ion batteries. We develop $NaNi_{0.5}Co_{0.5}O_2$ and $NaNi_{0.5}Fe_{0.5}O_2$, and contrast how different redox reactions can lead to different structural evolution upon desodiation.

2. Methods

2.1. Synthesis

To obtain stoichiometric compositions, 20% excess Na_2O (80%, Alfa Aesar) was measured with stoichiometric amounts of NiO (99%, Alfa Aesar) and Co_3O_4 (99%, Alfa Aesar) for $NaNi_{0.5}Co_{0.5}O_2$ and stoichiometric amounts of NiO and Fe_2O_3 (99.9%, Alfa Aesar) for $NaNi_{0.5}Fe_{0.5}O_2$. The precursors were ball-milled at 500 rpm for 4 h in sealed zirconia containers and fired under flowing O_2 at 800 °C for $NaNi_{0.5}Co_{0.5}O_2$ and 900 °C for $NaNi_{0.5}Fe_{0.5}O_2$. The samples were quenched to room temperature and transferred to an argon-filled glovebox. The target stoichiometry after firing was confirmed by inductively coupled plasma emission spectroscopy (ICP, Luvak Inc.) for both compositions.

2.2. Characterization

X-ray diffraction (XRD) patterns were recorded using a PANalytical X'Pert Pro X-ray diffractometer in the 2θ range from 5° to 85° using Cu Kα radiation. All the XRD samples were sealed with a Kapton film to avoid air exposure. To determine the structural parameters, Rietveld refinement was performed using X'Pert Highscore Plus software: the scale factor, peak profile parameters, lattice constants, atomic coordinates, and preferred orientation were refined step-by-step to achieve the best fit. The site occupancy factors were not refined, and we do not consider cation disorder between Na and transition metals due to their significant size differences.

The particle morphology was observed by field-emission scanning electron microscopy (FE-SEM, Zeiss Gemini Ultra-55). A thin layer of Pt was coated on the SEM samples to prevent charging. The oxidation states of transition metals were estimated by electron energy loss spectroscopy (EELS, 0.5 eV dispersion) combined with transmission electron microscopy (TEM, Philips CM200/FEG, 200 keV) in the diffraction mode. The spectra were collected from many different particles per specimen to obtain average results.

2.3. Battery test

The cathode was prepared by manually mixing 80 wt% active material, 15 wt% carbon black (Timcal, Super P), and 5 wt% polytetrafluoroethylene (DuPont, Teflon 8A). The mixture was rolled on a stainless steel plate and punched with holes of 7.94 mm diameter. The fabricated film had a loading density of $\sim$2.5 mg cm^{-2}. A Swagelok-type half-cell was assembled with the cathode film, Na metal (Sigma-Aldrich) as the anode, ethylene carbonate (EC, BASF)–diethyl carbonate (DEC, BASF) solution with $NaPF_6$ (98%, Sigma Aldrich) as the electrolyte, and glass fiber as the separator. The electrolyte was prepared by dissolving 1 M $NaPF_6$ in EC : DEC (1 : 1 ratio by volume), in which the moisture level was less than 3 ppm. The cells were cycled at room temperature (RT) using a Solartron 1470E operating in galvanostatic mode, assuming a 1C rate of 235 mA g^{-1} for $NaNi_{0.5}Co_{0.5}O_2$ and 238 mA g^{-1} for $NaNi_{0.5}Fe_{0.5}O_2$. The potentiostatic intermittent titration test (PITT) was carried out to obtain quasi-equilibrium voltage profiles with respect to the Na contents as well as current responses as a function of time. For every 10 mV in the given voltage windows, a constant voltage was applied until the current reached the C/50 level.

2.4. *In situ* XRD

To monitor the structural evolution of $NaNi_{0.5}Co_{0.5}O_2$ and $NaNi_{0.5}Fe_{0.5}O_2$ during electrochemical cycling, *in situ* XRD was performed on a Bruker D8 Advance diffractometer in the 2θ range from 6.5° to 30° using Mo Kα radiation. By using our custom-made cell with a beryllium window, the cathode was cycled at a C/24 rate on a Solartron 1287 potentiostat, and XRD patterns were collected every 20 minutes, equivalent to a resolution of approximately 1.4% Na per formula unit.

2.5. Computation

Density functional theory (DFT) calculations were performed using the Vienna *ab initio* simulation package (VASP) within the projector augmented-wave approach,[50,51] utilizing the Perdew–Burke–Ernzerhof (PBE) generalized gradient approximation (GGA) and Heyd–Scuseria–Ernzerhof (HSE06) approximation to the exchange–correlation energy functional.[52–55] U parameters of 3.4, 4.0, and 6.0 eV were assigned to Co, Fe, and Ni, respectively, in PBE calculations to correct for the self-interaction present in the functional. The values of the U parameters were determined following the approach of Jain *et al.*[56] A plane-wave energy cutoff of 520 eV and a k-point density of at least 1000 per number of atoms in a unit cell were used to ensure that all the calculations are converged to within 1 meV per atom.[57] All the calculations were spin-polarized, and the transition metals were initialized from a low-spin configuration except for Fe. For $NaNi_{0.5}Co_{0.5}O_2$ and $NaNi_{0.5}Fe_{0.5}O_2$, we selected up to 25 transition metal orderings with the lowest electrostatic energies, determined *via* Ewald summation, as implemented in the pymatgen library.[58] For each $x = 0$, 0.5, and 1 in $Na_{1-x}Ni_{0.5}Co_{0.5}O_2$ and $Na_{1-x}Ni_{0.5}Fe_{0.5}O_2$, the Na/vacancy ordering was determined by

the same enumeration and electrostatic ranking approach while keeping the lowest transition metal orderings that are determined for $NaNi_{0.5}Co_{0.5}O_2$ and $NaNi_{0.5}Fe_{0.5}O_2$. The supercell size was $2a \times 2b \times 1c$. Due to the computational expense of HSE calculations, all orderings were first relaxed using the PBE functional. The lowest energy orderings of each compound were then relaxed within HSE, under the assumption that the lowest energy structure is the same in both functionals.

3. Results

3.1. Synthesis of O3-$NaNi_{0.5}Co_{0.5}O_2$ and O3-$NaNi_{0.5}Fe_{0.5}O_2$

Fig. 1a and b show Rietveld-refined XRD profiles of the as-prepared $NaNi_{0.5}Co_{0.5}O_2$ and $NaNi_{0.5}Fe_{0.5}O_2$, respectively. For both compounds, all the indexed peaks correspond to the ordered rock-salt structure with O3-type layer stacking ($R\bar{3}m$ symmetry), suggesting that Co and Fe are well mixed with Ni in the 3b sites. The refinement results summarized in Table 1 and 2 indicate a hexagonal unit cell with lattice constants of a_h = 2.919 Å and c_h = 15.6441 Å for $NaNi_{0.5}Co_{0.5}O_2$ and a_h = 2.989 Å and c_h = 15.9236 Å for $NaNi_{0.5}Fe_{0.5}O_2$. The Na–O (6×) and (Ni/Co)–O (6×) distances in $NaNi_{0.5}Co_{0.5}O_2$ are determined to be 2.283 Å and 1.968 Å, respectively, and the Na–O (6×) and (Ni/Fe)–O (6×) distances in $NaNi_{0.5}Fe_{0.5}O_2$ are 2.373 Å and 2.053 Å, respectively. The lattice parameters for the two materials are in good agreement with the literature.[59,60]

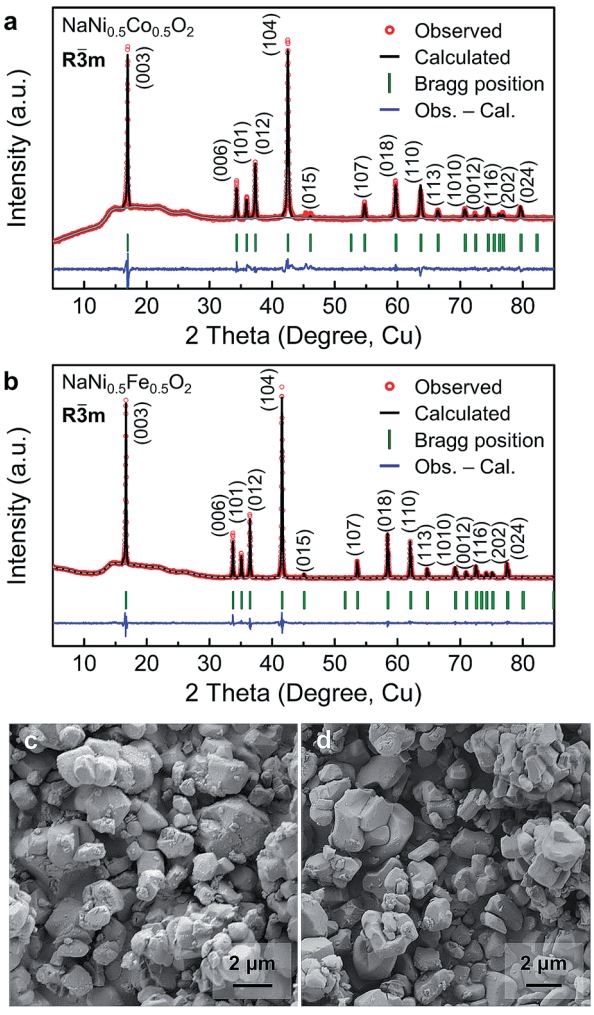

Fig. 1 Rietveld-refined XRD profiles of the as-synthesized (a) $NaNi_{0.5}Co_{0.5}O_2$ and (b) $NaNi_{0.5}Fe_{0.5}O_2$. Note that the broad background between 10° and 30° is due to a polyimide (Kapton) film sealing the sample. SEM images of the as-synthesized (c) $NaNi_{0.5}Co_{0.5}O_2$ and (d) $NaNi_{0.5}Fe_{0.5}O_2$ particles.

Although the conventional unit cell with the $R\bar{3}m$ symmetry is hexagonal, a monoclinic unit cell with the $C2/m$ symmetry is often used to determine a distortion of the O3 structure[59,61] as monoclinicity can be caused by Jahn-Teller distortion or transition metal ordering.[62] As illustrated in Fig. S1 (ESI†), the conversion operation from hexagonal (h) to monoclinic (m) unit cell is $a_m = \sqrt{3}\ a_h$, $b_m = b_h$, and $c_m = c_h\ (3 \sin \beta)^{-1}$. Thus, the degree of distortion can be estimated by calculating the a_m to b_m ratio and converting c_m into c_h with β. For the as-synthesized $NaNi_{0.5}Co_{0.5}O_2$ and $NaNi_{0.5}Fe_{0.5}O_2$, the a_m to b_m ratios are 1.736 and 1.733 with $\beta = 107.94°$ and 107.92°, respectively, suggesting that both are unlikely to be distorted. This implies that Co and Fe substitution for Ni can suppress the long-range monoclinic distortion observed in $NaNiO_2$. The lattice parameters of $NaNi_{0.5}Co_{0.5}O_2$ and $NaNi_{0.5}Fe_{0.5}O_2$ obtained from Rietveld refinement using the $C2/m$ symmetry are summarized in ESI, Table S1.† Fig. 1c and d show the SEM images of $NaNi_{0.5}Co_{0.5}O_2$ and $NaNi_{0.5}Fe_{0.5}O_2$, respectively. Average particle sizes for both materials are ~1 μm.

3.2. Battery test

Fig. 2a shows the voltage of $NaNi_{0.5}Co_{0.5}O_2$ as a function of the specific capacity at a C/10 rate. The charge/discharge capacities achieved in the voltage window of 2.0–4.2 V are 146/115, 115/114, 115/113, and 113/112 mA h g^{-1} in the first, second, fifth, and tenth cycles, respectively. Notable plateau-like features, which are equivalent to the peaks in the differential capacity *versus* voltage ($dQ\ dV^{-1}$) plot in the inset, consistently appear at 2.49 and 3.84 V upon charging and at 2.34 and 3.75 V upon discharging in multiple cycles, implying similar reversible two-phase reaction paths for desodiation and sodiation. Fig. 2b shows the quasi-equilibrium voltage profile of $NaNi_{0.5}Co_{0.5}O_2$ with respect to the Na contents obtained from PITT at RT. When charged to 4.2 V, 0.61 Na per formula unit (144 mA h g^{-1}) can be extracted, and 0.54 Na (127 mA h g^{-1}) can be reinserted in the

Table 1 Rietveld refinement results for $NaNi_{0.5}Co_{0.5}O_2$[a]

Atom	Site	*x*	*y*	*z*	SOF
Na	3a	0	0	0	1
Ni	3b	0	0	0.5	0.5
Co	3b	0	0	0.5	0.5
O	6c	0	0	0.2335	1

[a] Space group: $R\bar{3}m$; unit cell: $a_h = b_h$ = 2.919 Å, c_h = 15.6441 Å, $\alpha = \beta = 90°$, $\gamma = 120°$; volume = 115.406 Å^3; radiation λ = 1.5406 Å, $5° < 2\theta < 85°$; scale factor: 0.029844; preferred orientation: 0.993047; overall B-factor: 0.270232, U = 0.030592, V = 0.047122, W = 0.020897; pseudo-Voigt fit, R_{wp} = 1.51369, R_p = 0.9442, χ^2 = 7.40981.

Table 2 Rietveld refinement results for $NaNi_{0.5}Fe_{0.5}O_2$[a]

Atom	Site	x	y	z	SOF
Na	3a	0	0	0	1
Ni	3b	0	0	0.5	0.5
Fe	3b	0	0	0.5	0.5
O	6c	0	0	0.2336	1

[a] Space group: $R\bar{3}m$; unit cell: $a_h = b_h = 2.989$ Å, $c_h = 15.9236$ Å, $\alpha = \beta = 90°$, $\gamma = 120°$; volume = 123.171 Å^3; radiation $\lambda = 1.5406$ Å, $5° < 2\theta < 85°$; scale factor: 0.037514; preferred orientation: 0.95460; overall B-factor: 0.424858, $U = 0.0286$, $V = 0.00774$, $W = 0.01509$; pseudo-Voigt fit, $R_{wp} = 2.22108$, $R_p = 1.4155$, $\chi^2 = 10.9334$.

subsequent discharge to 2.0 V. $NaNi_{0.5}Co_{0.5}O_2$ also shows good rate capability (Fig. S2a, ESI†), delivering ~100 mA h g^{-1} at the 1C discharge rate.

Fig. 2c plots the discharge cyclability of $NaNi_{0.5}Co_{0.5}O_2$ in the range of 2.0–4.2 V at various temperatures. The capacity delivered in the first cycle at RT (115 mA h g^{-1}) increases as the temperature increases to 40 °C (124 mA h g^{-1}) and 55 °C (139 mA h g^{-1}). At RT and 40 °C the capacity decay per cycle is 0.4% and 0.5%, respectively. At 55 °C, more pronounced capacity fading (1% decay per cycle) occurs. As shown in Fig. 2d, cycling $NaNi_{0.5}Co_{0.5}O_2$ with an expanded voltage window (2.0–4.5 V) leads to slightly higher initial discharge capacities at each temperature. However, the capacities fade rapidly in the first five cycles at the higher temperatures. The full charge and discharge voltage profiles of $NaNi_{0.5}Co_{0.5}O_2$ for 20 cycles obtained under these various conditions are shown in Fig. S3, ESI.† Also, capacity retention over an extended number of cycles (4.2 V cutoff, RT) is plotted in Fig. S4a.†

Fig. 3a shows the voltage profiles of $NaNi_{0.5}Fe_{0.5}O_2$ with respect to the specific capacity at a C/10 rate. The cell was cycled between 2.0 and 3.9 V, and the charge/discharge capacities in the first, second, fifth, and tenth cycles are 156/129, 144/128, 138/126, and 128/126 mA h g^{-1}, respectively. Compared with a previous study on $NaNi_{0.5}Fe_{0.5}O_2$, in which $NaClO_4$ in propylene carbonate was used as the electrolyte,[60] we observe a similar voltage profile but slightly improved capacity with reasonable retention in a larger voltage window. If the $NaNi_{0.5}Fe_{0.5}O_2$ cathode is charged at 4.2 V, the same cutoff as that used for the $NaNi_{0.5}Co_{0.5}O_2$ cycling, a substantial amount of Na can be extracted (189 mA h g^{-1}) in the first cycle; however, the capacity decays abruptly in subsequent cycles, as demonstrated in the inset. By charging to 3.9 V, 0.64 Na (152 mA h g^{-1}) is extracted from $NaNi_{0.5}Fe_{0.5}O_2$, and 0.61 Na (145 mA h g^{-1}) can be inserted back upon discharge to 2.0 V according to the PITT (Fig. 3b). The rate capability of the $NaNi_{0.5}Fe_{0.5}O_2$ cathode is shown in Fig. S2b, ESI.† At the 1C discharge rate, the cathode delivers ~95 mA h g^{-1}.

The cycling properties of $NaNi_{0.5}Fe_{0.5}O_2$ at various temperatures with the two different voltage cutoffs are plotted in Fig. 3c and d. With a cutoff of 3.9 V (Fig. 3c), the capacity fade is minor at RT (after 20 cycles, 0.3% decay per cycle) and 40 °C (after 20 cycles, 0.4% decay per cycle). Noticeably, the initial discharge capacity at 55 °C is not only smaller than that at 40 °C but also decays faster (after 20 cycles, 0.6% decay per cycle). Fig. 3d

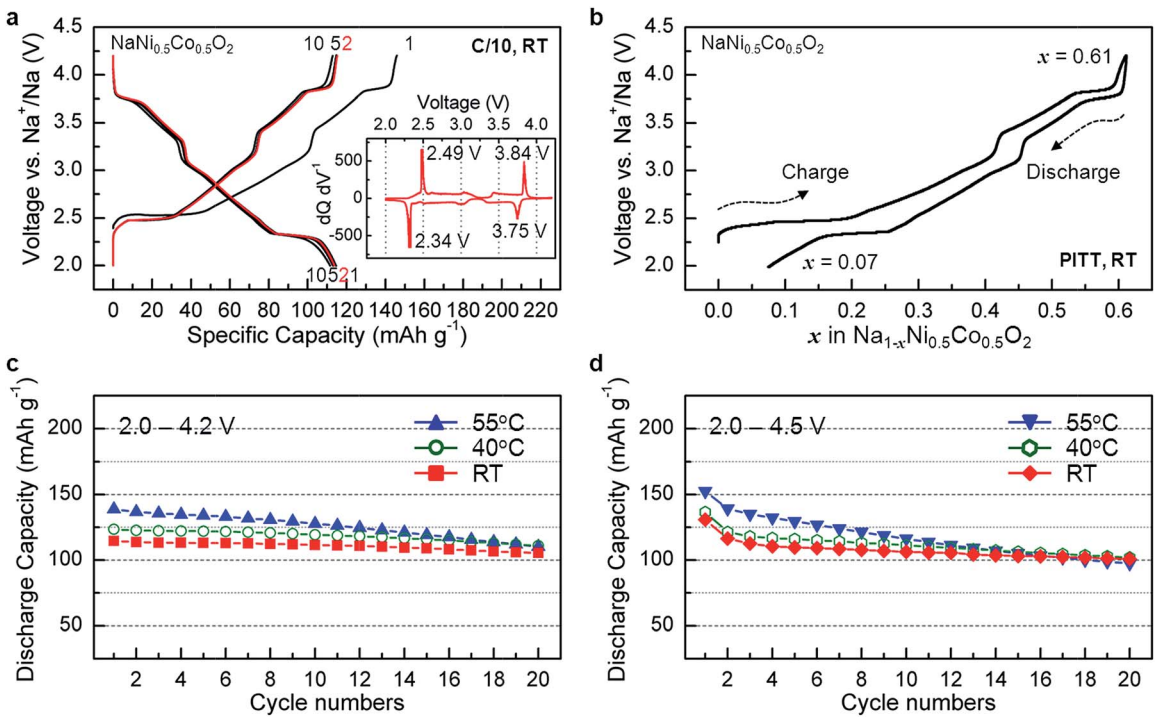

Fig. 2 Voltage curves of the $NaNi_{0.5}Co_{0.5}O_2$ cathode as a function of (a) specific capacity at galvanostatic C/10 cycling (inset: differential capacity *versus* voltage plot in the second cycle) and (b) Na contents determined from the PITT, and cycling performance of $NaCo_{0.5}Ni_{0.5}O_2$ at various temperatures between (c) 2.0 and 4.2 V and (d) 2.0 and 4.5 V.

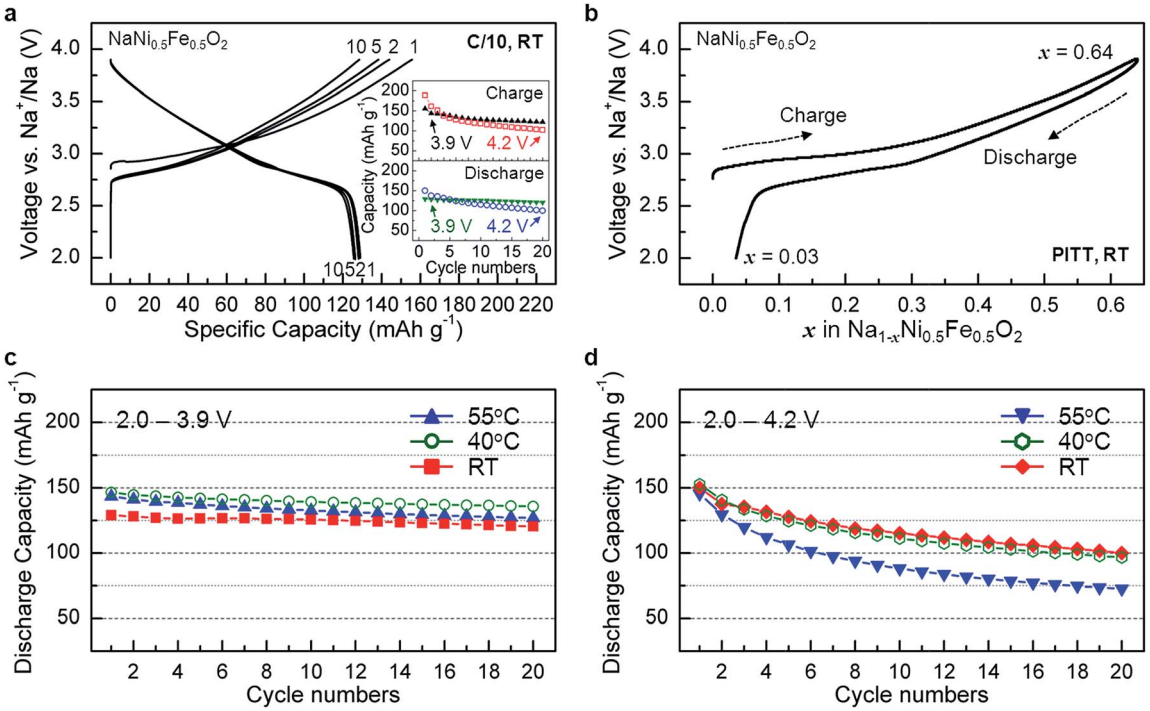

Fig. 3 Voltage curves of the $NaNi_{0.5}Fe_{0.5}O_2$ cathode as a function of (a) specific capacity at galvanostatic C/10 cycling (inset: capacity retention at charge (top) and discharge (bottom) with two different cutoffs) and (b) Na contents determined from the PITT, and cycling performance of $NaNi_{0.5}Fe_{0.5}O_2$ at various temperatures between (c) 2.0 and 3.9 V and (d) 2.0 and 4.2 V.

demonstrates that the 4.2 V cutoff leads to poor capacity retention at all temperatures. The initial capacities (~150 mA h g^{-1}) do not vary much with temperature. The fading rates at RT and 40 °C (1.7% and 1.8% decay per cycle, respectively) are similar, whereas the capacity at 55 °C decreases steeply during the 20 cycles at a decay rate of 2.5% per cycle. The full charge and discharge voltage profiles under the various conditions and capacity retention over 150 cycles of $NaNi_{0.5}Co_{0.5}O_2$ are shown in Fig. S5 and S4b (ESI†), respectively.

Since the $NaNi_{0.5}Co_{0.5}O_2$ system has several pronounced plateaus, we use PITT with a small potentiostatic step (10 mV) to investigate the current relaxation on these plateaus (Fig. 4a). Assuming that Na intercalation occurs without parasitic reactions, the current measured by PITT is proportional to the rate of phase transformation.[63] In the plateau regions around 2.5 and 3.8 V for $NaNi_{0.5}Co_{0.5}O_2$ in Fig. 4a, the current is initially the highest within the 10 mV step and then monotonically decreases with time. In general, this behavior is indicative of a phase transformation, which does not require a barrier for nucleation. The plateau at 2.5 V likely reflects a stacking transition from the O3- to P3-type phase as the P3-type structure, in which Na occupies the prismatic site created by the transition metal layer gliding from the O3-type structure, becomes the most stable upon desodiation.[64] This O3- to P3-type phase transition is reversible and has also been observed in many O3-$NaMO_2$ compounds (M = Cr, Mn, Co, Ni, $Ni_{0.5}Mn_{0.5}$, $Ni_{2/3}Sb_{1/3}$, $Mn_{0.25}Fe_{0.25}Co_{0.25}Ni_{0.25}$).[36–41,47,65]

The plateau of $Na_{1-x}Ni_{0.5}Fe_{0.5}O_2$ in the $0.05 < x < 0.3$ range is less pronounced in Fig. 4b compared with that of $Na_{1-x}Ni_{0.5}Co_{0.5}O_2$. However, the current profile still exhibits a similar relaxation response, suggesting that desodiated $Na_{1-x}Ni_{0.5}Fe_{0.5}O_2$ also undergoes the O3–P3 transition at around $x = 0.25$, as similarly reported by Wang *et al.*[60] Upon further charging ($x > 0.4$), Na extraction appears to occur topotactically without any indication of a phase transition, leading to a smoothly increasing voltage curve.

3.3. *In situ* XRD

To better investigate the structural evolution of $NaNi_{0.5}Co_{0.5}O_2$ and $NaNi_{0.5}Fe_{0.5}O_2$ during electrochemical cycling, we performed *in situ* XRD. The results are shown in Fig. 5. For $NaNi_{0.5}Co_{0.5}O_2$, charge and discharge capacities obtained between 4.2 and 2 V are 145 and 115 mA h g^{-1}, which are approximately 64% and 49% of the theoretical capacity, respectively. The results in Fig. 5a indicate that when a small amount ($x = 0.04$) of Na is extracted from $Na_{1-x}Ni_{0.5}Co_{0.5}O_2$ (O3 structure), the intensity of the $(003)_h$ peak at 7.8° and the $(104)_h$ peak at 19.2° is reduced while new peaks grow at 7.5° and 19.75°. According to Rietveld refinement using the *C*2/*m* symmetry, the new structure also has O3-type stacking, but the ratio between the a_m and b_m lattice parameters significantly deviates from $\sqrt{3}$, yielding reduced symmetry (Table S2, ESI†). This is indicative of a monoclinic distortion (O′3 structure), and the peaks can be indexed to $(001)_m$ at 7.5°, and $(111)_m$ at 19.75°. Upon further desodiation, the O′3-phase disappears, and different peaks emerge at 7.3° for $x = 0.16$ and at around 20.7° for $x = 0.24$. The peaks represent typical P3-type stacking with a monoclinic distortion (P′3 structure).[48,66] Structure parameters

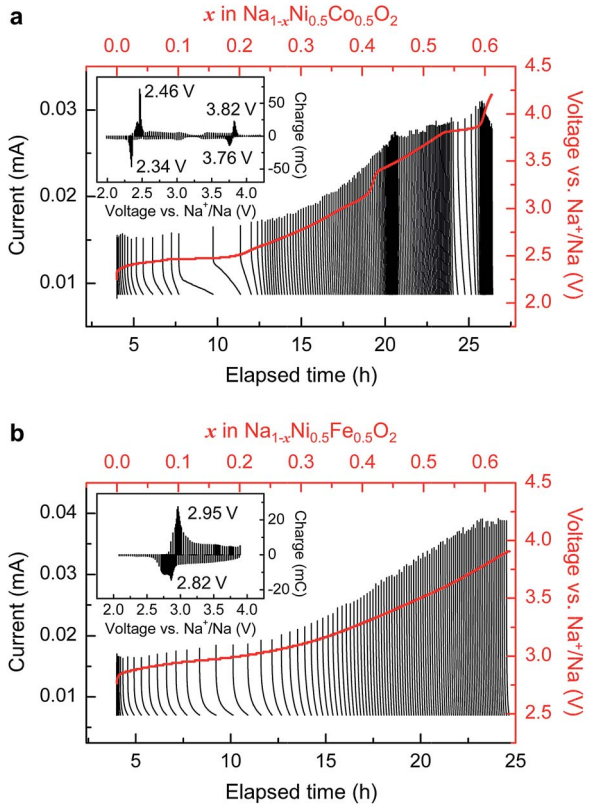

Fig. 4 Current *versus* elapsed time profiles and the corresponding voltage *versus* Na content profiles obtained from PITT with 10 mV increments in (a) $NaNi_{0.5}Co_{0.5}O_2$ and (b) $NaNi_{0.5}Fe_{0.5}O_2$ at RT. The insets present charge *versus* voltage diagrams of each compound.

refined with this hypothesis are given in Table S2.† For $0.16 < x < 0.34$, the peaks at 7.3° and around 20.7° are assigned to $(001)_m$ and to $(11\bar{2})_m$ and $(201)_m$ planes in the P′3 lattice. Note that the monoclinic distortion observed in intermediate O′3 and P′3 phases is consistent with the results reported by Saddoune *et al.*[59] As desodiation continues, the $(001)_m$ peak turns into a $(003)_h$ peak, and the $(11\bar{2})_m$ and $(201)_m$ peaks merge into a single hexagonal $(015)_h$ peak, forming a P3 structure at $x = 0.34$. The $(003)_h$ peak gradually shifts to a lower angle, indicating that the distance between transition metal layers increases with Na extraction. The P3 structure develops a monoclinic distortion (P″3 structure) once more between $x = 0.42$ and 0.57 with the $(015)_h$ peak splitting into $(11\bar{2})_m$ and $(201)_m$. This P″3 structure returns to a distorted O3-type structure at the end of charge ($x > 0.61$), but the lattice parameters vary from those of the O3 and O′3 phases (*i.e.*, O″3 structure) that occur at a higher Na content.

The overall phase transition in $Na_{1-x}Ni_{0.5}Co_{0.5}O_2$ ($0 < x < 0.64$) is reversible. The diffraction pattern is almost identical at the same Na content on charge and discharge. However, it should be noted that incomplete re-sodiation at 2 V results in the O′3 phase remaining at the end of discharge. The initial O3 structure is recovered only when discharging to 1 V, as shown in Fig. S6.† Hence our *in situ* study shows that the $Na_{1-x}Ni_{0.5}Co_{0.5}O_2$ system reversibly goes through three distinct O3-type and three distinct P3-type phases.

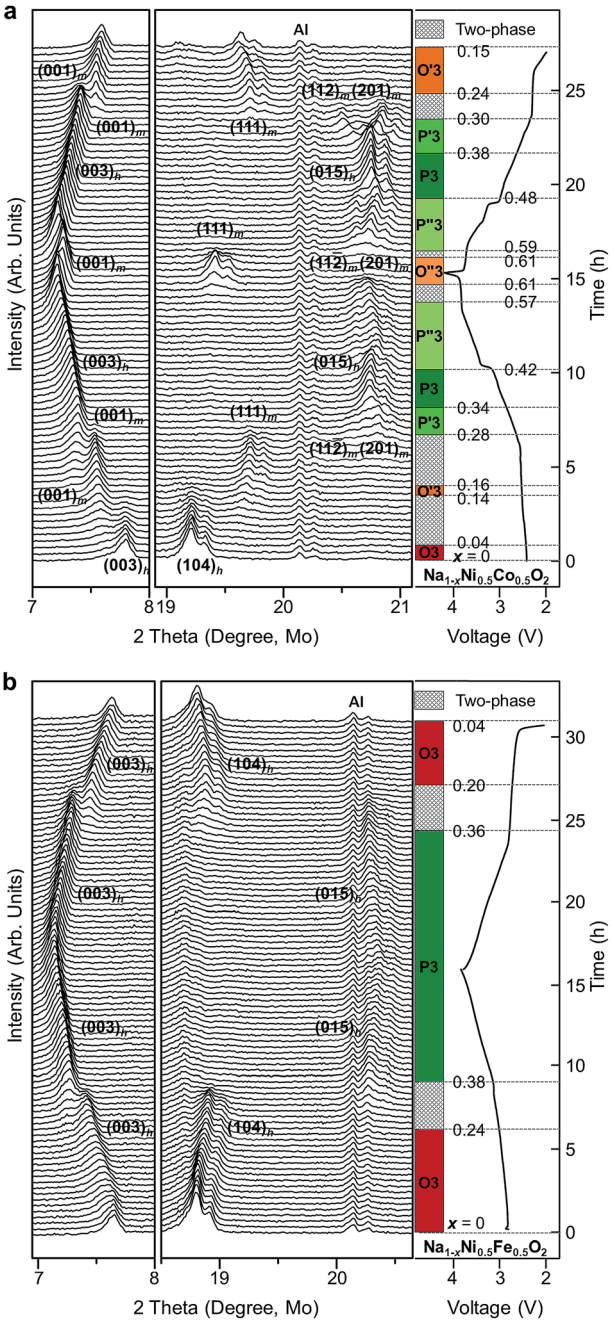

Fig. 5 *In situ* XRD patterns of (a) $NaNi_{0.5}Co_{0.5}O_2$ cycled from 4.2 to 2 V and (b) $NaNi_{0.5}Fe_{0.5}O_2$ cycled from 3.9 to 2 V at a C/24 rate. The double peak is due to Mo $K\alpha_1$ and $K\alpha_2$ radiation.

In the *in situ* test of $Na_{1-x}Ni_{0.5}Fe_{0.5}O_2$, 0.66 Na is extracted from the cathode (159 mA h g^{-1}) and 0.62 Na is inserted back (145 mA h g^{-1}) upon cycling between 3.9 and 2 V at a C/24 rate. The results are shown in Fig. 5b. The $(003)_h$ and $(104)_h$ peaks for the O3 phase shift toward a lower and higher angle upon desodiation ($x < 0.24$), respectively. These peaks gradually disappear as new peaks, which are indexed to $(003)_h$ and $(015)_h$ for a P3 phase, emerge in the range $0.24 < x < 0.38$ (*i.e.* O3–P3 two-phase region). We do not observe any lattice distortion along the phase transition from O3 to P3, and the P3 structure prevails

in the range $0.38 < x < 0.66$. The overall phase evolution is reversible upon sodiation: XRD patterns obtained are symmetrical for charge and discharge.

Fig. 6 shows a contour plot (bird's eye view) of peak intensity for the *in situ* XRD data and allows us to more qualitatively compare both systems. In Fig. 6a, three distinct two-phase reactions can be observed for $Na_{1-x}Ni_{0.5}Co_{0.5}O_2$ at around $x =$ 0.1, 0.2, and 0.59, corresponding to the O3–O′3, O′3–P′3, and P″3–O″3 transitions, respectively. As a result, the plateaus near 2.5 V can be assigned to two two-phase (O3–O′3 and O′3–P′3) reactions. The P″3–O″3 reaction occurs at ≈3.8 V, consistent with the PITT result in Fig. 4a. In contrast, $Na_{1-x}Ni_{0.5}Fe_{0.5}O_2$ in Fig. 6b undergoes a two-phase reaction between the O3 and P3 for $0.24 < x < 0.38$, corresponding to the 3 V plateau in Fig. 4b. It is possible that there is a minor phase transition for a very low level of Na extraction from $Na_{1-x}Ni_{0.5}Fe_{0.5}O_2$. This can be seen in Fig. 5b and in an enlargement in Fig. S7† which shows an abrupt change in the rate of peak shifting with the desodiation level. However, we cannot fully resolve this phase transition. As the lattice parameter variation is almost continuous with desodiation, maintaining $R\bar{3}m$ symmetry (Table S3†), we denote this as one O3 structure field. The *in situ* XRD results clearly demonstrate how the structure of $Na_{1-x}Ni_{0.5}Co_{0.5}O_2$ and $Na_{1-x}Ni_{0.5}Fe_{0.5}O_2$ and their voltage profiles are differently affected by the Na content. We discuss the origin of these changes in more detail later in the paper. The overall lattice parameter evolution upon desodiation and re-sodiation for the two compounds is plotted in Fig. S8, ESI.†

3.4. Oxidation states of transition metals

We investigate how the transition metal valence in $NaNi_{0.5}Co_{0.5}O_2$ and $NaNi_{0.5}Fe_{0.5}O_2$ changes with respect to the Na content. By calculating the (*ab initio*) energy of a large number of transition metal configurations and magnetic states at each composition in Table 3,[58,67] we report results for total magnetic moments on Ni, Co, and Fe in the lowest energy configurations. The magnetic moments of Ni and Co in $NaNi_{0.5}Co_{0.5}O_2$ in the low-spin configuration are 0.893 and $0.021\mu_B$, respectively, in agreement with the expectation of Ni^{3+} ($e_g^1t_{2g}^6$) and Co^{3+} ($e_g^0t_{2g}^6$) electron configurations.[68] Similarly, Ni and Fe are

Table 3 Total magnetic moment (oxidation state) of $Na_{1-x}Ni_{0.5}Co_{0.5}O_2$ and $Na_{1-x}Ni_{0.5}Fe_{0.5}O_2$ ($x = 0$, 0.5, and 1)

	Total magnetic moment (oxidation state)			
	$Na_{1-x}Ni_{0.5}Co_{0.5}O_2$		$Na_{1-x}Ni_{0.5}Fe_{0.5}O_2$	
x	Ni	Co	Ni	Fe
0	$0.893\mu_B$ (Ni^{3+})	$0.021\mu_B$ (Co^{3+})	$0.941\mu_B$ (Ni^{3+})	$4.192\mu_B$ (Fe^{3+})
0.5	$0.000\mu_B$ (Ni^{4+})	$0.000\mu_B$ (Co^{3+})	$0.897\mu_B$ (Ni^{3+})	$3.463\mu_B$ (Fe^{4+})
1	$0.025\mu_B$ (Ni^{4+})	$1.124\mu_B$ (Co^{4+})	$0.086\mu_B$ (Ni^{4+})	$3.544\mu_B$ (Fe^{4+})

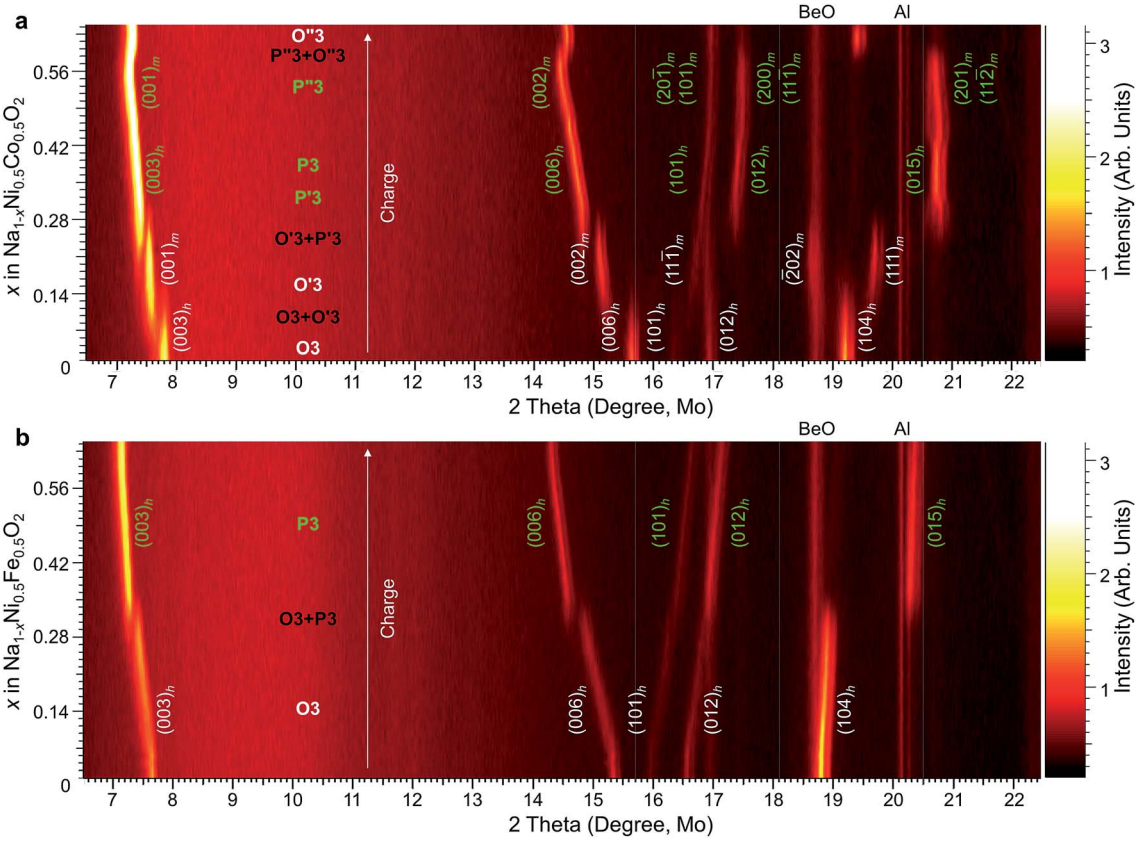

Fig. 6 Intensity contour maps (bird's eye view) of the *in situ* XRD patterns of (a) $NaNi_{0.5}Co_{0.5}O_2$ and (b) $NaNi_{0.5}Fe_{0.5}O_2$ in the 1st charge.

approximately trivalent in $NaNi_{0.5}Fe_{0.5}O_2$ with computed magnetic moments of Ni (low-spin) and Fe (high-spin) of 0.941 ($e_g^1t_{2g}^6$) and 4.192μ_B ($e_g^2t_{2g}^3$), respectively.[69] Note that underestimation of the total magnetic moment in DFT is typical and due to the surrounding oxygen ions sharing a portion of the moment as a result of hybridization.[70,71]

When removing 0.5 Na from $Na_{1-x}Ni_{0.5}Co_{0.5}O_2$, the magnetic moment of Ni^{3+} drops to 0μ_B, corresponding to the Ni^{4+} configuration ($e_g^0t_{2g}^6$), whereas the magnetic moment of Co^{3+} remains almost unchanged. The oxidation state of Co becomes tetravalent with a magnetic moment of 1.124μ_B ($e_g^0t_{2g}^5$) in the fully desodiated state (Na = 0). Na extraction from $NaNi_{0.5}Fe_{0.5}O_2$ to $Na_{0.5}Ni_{0.5}Fe_{0.5}O_2$ reduces the magnetic moment of Fe^{3+} to 3.463μ_B, indicating tetravalency in the high spin configuration ($e_g^1t_{2g}^3$), while that of Ni^{3+} does not vary much until the material is completely desodiated.

To support our computational results, we performed *ex situ* EELS on the electrochemically desodiated $Na_{1-x}Ni_{0.5}Co_{0.5}O_2$ and $Na_{1-x}Ni_{0.5}Fe_{0.5}O_2$ cathodes (x = 0, 0.25, and 0.5). The area ratio between the L3 and L2 peaks in the spectra with baseline subtraction was calculated for each transition metal to determine the variation of oxidation states, as reported by Graetz *et al.* and Tan *et al.*[72,73] In Fig. 7a, the L3/L2 area ratio for Ni increases upon desodiation whereas that for Co remains almost invariant in $Na_{1-x}Ni_{0.5}Co_{0.5}O_2$. This is indicative of Ni^{3+} oxidation in x < 0.5. In contrast, it is not Ni but Fe in $Na_{1-x}Ni_{0.5}Fe_{0.5}O_2$ (Fig. 7b) that shows a substantial change in the L3/L2 ratio: the ratio for Fe decreases upon desodiation while that for Ni slightly increases. The result implies that Fe^{3+} oxidation is responsible for most of the electrochemical activity in x < 0.5 although partial oxidation of Ni^{3+} can also occur. The EELS results agree well with our computational data. Still, it is important to note that our average EELS results may end up representing local areas of the cathode particles. The redox reaction may vary by the local environment in mixed transition metal systems.

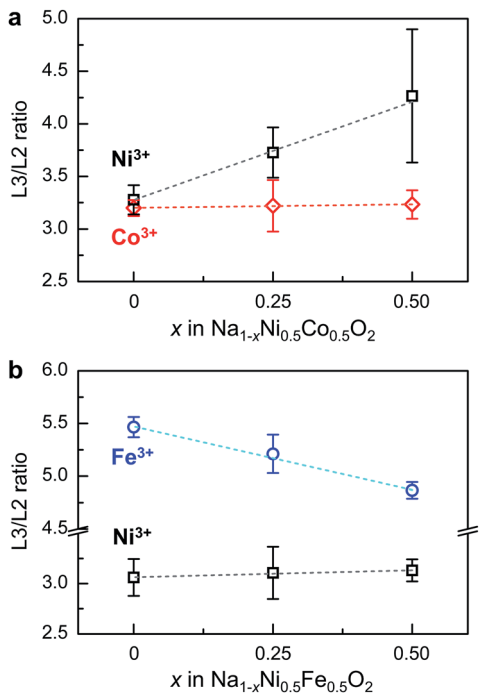

Fig. 7 Area ratios between L3 and L2 peaks in the electron energy loss spectra of (a) Ni and Co in (a) $Na_{1-x}Ni_{0.5}Co_{0.5}O_2$ and (b) Ni and Fe in $Na_{1-x}Ni_{0.5}Fe_{0.5}O_2$ with respect to x = 0, 0.25, and 0.5.

4. Discussion

The oxidation states calculated in Table 3 provide insight into how the redox reaction proceeds. In $NaNi_{0.5}Co_{0.5}O_2$, Ni^{3+} oxidation occurs prior to Co^{3+} oxidation, as also observed in $NaNi_{0.6}Co_{0.4}O_2$,[59] $LiNi_{0.8}Co_{0.2}O_2$,[74] and $Li(Ni_{1/3}Co_{1/3}Mn_{1/3})O_2$.[68] In $NaNi_{0.5}Fe_{0.5}O_2$, Fe^{3+} oxidation precedes the Ni^{3+} reaction similar to $LiNi_{1-y}Fe_yO_2$.[75] While it is possible that the different redox behavior, as suggested in Table 3, may account for the difference in structural evolution between the two compounds, it is not exactly clear how this mechanism would operate.[60,76–81]

The difference in phase transitions seen in $Na_{1-x}Ni_{0.5}Co_{0.5}O_2$ as compared to $Na_{1-x}Ni_{0.5}Fe_{0.5}O_2$ is remarkable. While both systems undergo a generic O3–P3 transition at partial desodiation, similar to what has been observed in many layered Na-oxides,[36–41,47,65] the $Na_{1-x}Ni_{0.5}Co_{0.5}O_2$ system also shows several monoclinically distorted versions of O3 and P3. These are likely due to Na-vacancy ordering caused by the strong Na–Na interactions[82] which are much more pronounced than in the equivalent Li systems. One can for example compare the voltage curve of O3-$LiCoO_2$ with that of O3-$NaCoO_2$.[61,82,83] Many more ordered phases and associated voltage steps occur in a Na system than in the corresponding Li system. In general, mixing of transition metals leads to strong electrostatic perturbations on the alkali sublattice, thereby suppressing ordering. This is why few Li-vacancy orderings are found in layered Li compounds with mixed transition metals. In Na systems the ordering sometimes survives the perturbation from the transition metal mixing as it appears to be the case in the $Na_{1-x}Ni_{0.5}Co_{0.5}O_2$ system. Because Ni^{3+} and Co^{3+} energy states are closer in energy, and their partial oxidation can even lead to metallic-like, delocalized states,[68,84] the charge density in the transition metal layer of the $Na_{1-x}Ni_{0.5}Co_{0.5}O_2$ system is more homogeneous than that in the $Na_{1-x}Ni_{0.5}Fe_{0.5}O_2$ material, where the perturbation of the random Ni and Fe arrangement is strong enough to destroy long range ordering on the Na-vacancy sublattice.

The two materials have different structural stabilities in the charged state. This can be qualitatively elucidated by cycling at elevated temperatures and/or in a wide voltage window. The discharge capacity in Fig. 2c noticeably increases as the temperature increases. This may indicate transport limitations in $NaNi_{0.5}Co_{0.5}O_2$ at the end of discharge. Thus, a larger Na intercalation activity can also be expected when reducing the particle size. In addition, capacity fading at 55 °C suggests that the Na intercalation process may be somewhat limited by the stability of the desodiated structure, as has been reported in Li-ion batteries.[85] At each temperature, the capacity fading is larger if $NaNi_{0.5}Co_{0.5}O_2$ is cycled from 2.0 to 4.5 V (Fig. 2d) rather than from 2.0 to 4.2 V. The results imply that increasing the temperature as well as a high voltage cutoff can accelerate destabilization of the material. A more in-depth analysis of the

stability of layered Na-compounds with respect to the charged structure of O3-type $NaMO_2$ has been reported elsewhere.[82]

In $NaNi_{0.5}Fe_{0.5}O_2$, the Na intercalation activity increases with temperature from RT to 40 °C in 2.0–3.9 V. However, the discharge capacity does not increase when the temperature is increased from 40 °C and 55 °C, but decays faster, suggesting that $NaNi_{0.5}Fe_{0.5}O_2$ is less kinetically limited but more stability-limited, as compared to $NaNi_{0.5}Co_{0.5}O_2$. This behavior becomes more evident in cycling from 2.0 to 4.2 V, as shown in Fig. 3d. In this voltage range, the capacities are independent of temperature but decrease faster than in the 2.0–3.9 V range. Clearly, the material seems rapidly destabilized at voltages above 3.9 V, exhibiting severe capacity fade, especially at 55 °C. This instability is likely due to Fe^{4+} migration, resulting in an irreversible structural change.[60,64,86,87]

Fig. 8 shows how the structure of desodiated $Na_{1-x}Ni_{0.5}Fe_{0.5}O_2$ ($x > 0.65$) changes during overcharge from 3.9 to 4.2 V. *In situ* XRD patterns show that the P3 structure suddenly disappears above 3.9 V. The $(003)_h$ peak at 7.1° continuously shifts to a higher angle, indicating a decreasing inter-layer distance. In addition, the overall diffraction peaks become broad with decreasing intensity, implying a certain amount of disorder, possibly from stacking faults in the structure. Although the information obtainable by diffraction is insufficient to fully characterize this degradation process, the structural change can be related to Fe^{4+} migration, which has been previously pointed out in the literature to explain the degradation of compounds with a high amount of Fe.[59,86,88] The P3 structure does not reappear upon discharge, while the O3 structure emerges when sodiated below 2.5 V. This result confirms the irreversible structural change due to overcharge, and careful control of the voltage window is therefore necessary to cycle $NaNi_{0.5}Fe_{0.5}O_2$ without significant fade. Thus, the cyclability of $NaNi_{0.5}Fe_{0.5}O_2$ may be further improved by doping inactive tetravalent elements for Fe^{3+} as they can stabilize the charged structure, thereby minimizing the irreversible structural change. It has recently been suggested that the optimal Fe content in a compound is ~1/3 per formula unit as the Jahn-Teller distortion of Fe^{4+} assists mobility at the top of charge, but too high Fe content leads to Fe migration into the tetrahedral site.[89]

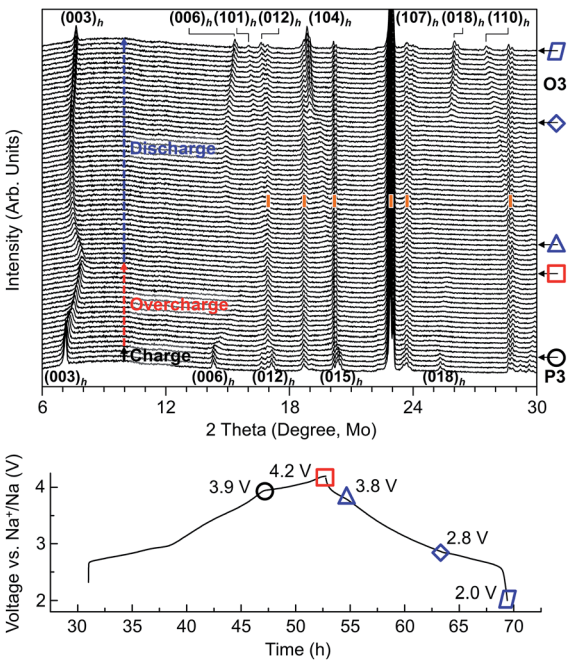

Fig. 8 *In situ* XRD patterns of $NaNi_{0.5}Fe_{0.5}O_2$ charged from 3.7 to 4.2 V and subsequently discharged to 2 V at a C/24 rate. Orange tick marks indicate peaks from *in situ* cell components.

5. Conclusion

In this work, we have synthesized O3-type $NaNi_{0.5}Co_{0.5}O_2$ and $NaNi_{0.5}Fe_{0.5}O_2$ using a solid-state method and investigated their electrochemical properties and associated structural evolution as positive electrode materials for rechargeable Na-ion batteries. Although they have an identical initial structure and both contain trivalent Ni, the voltage profiles of the two materials are qualitatively distinct from each other. The $NaNi_{0.5}Co_{0.5}O_2$ system shows a large number of well-defined phase transitions, while the $NaNi_{0.5}Fe_{0.5}O_2$ system only shows the typical O3–P3 transition. In $NaNi_{0.5}Co_{0.5}O_2$, cycling at higher temperature leads to further Na extraction and reinsertion, indicating that the capacity is rate limited. The capacity fade of $NaNi_{0.5}Fe_{0.5}O_2$ can be reduced by minimizing the irreversible structural change at the top of charge. Given that mixing of different transition metals leads to different structural evolution and associated redox response, results obtained in this study can be used to design desirable materials for Na-ion batteries.

Acknowledgements

This work was funded by the Samsung Advanced Institute of Technology. We used computational assets of the Extreme Science and Engineering Discovery Environment (XSEDE), which is supported by National Science Foundation grant no. ACI-1053575. We also utilized resources of the National Energy Research Scientific Computing Center (NERSC) and Molecular Foundry at Lawrence Berkeley National Laboratory, a DOE Office of Science User Facility supported by the Office of Science of the US Department of Energy under contract no. DE-C02-05CH11231.

References

1 M. S. Whittingham, *Chem. Rev.*, 2004, **104**, 4271–4302.
2 S. W. Kim, D. H. Seo, X. H. Ma, G. Ceder and K. Kang, *Adv. Energy Mater.*, 2012, **2**, 710–721.
3 M. S. Islam and C. A. J. Fisher, *Chem. Soc. Rev.*, 2014, **43**, 185–204.
4 M. Moradi, J. C. Kim, J. Qi, K. Xu, X. Li, G. Ceder and A. M. Belcher, *Green Chem.*, 2016, **18**, 2619–2624.
5 D. H. Kim, P. Muralidhara, H.-W. Lee, R. Ruffo, Y. Yang, C. K. Chan, H. Peng, R. A. Huggins and Y. Cui, *Nano Lett.*, 2008, **8**, 3948–3952.
6 G. Meligrana, C. Gerbaldi, A. Tuel, S. Bodoardo and N. Penazzi, *J. Power Sources*, 2006, **160**, 516–522.

7 J. Cho, Y. J. Kim and B. Park, *Chem. Mater.*, 2000, **12**, 3788–3791.
8 A. Vu, Y. Qian and A. Stein, *Adv. Energy Mater.*, 2012, **2**, 1056–1085.
9 K. Mizushima, P. C. Jones, P. J. Wiseman and J. B. Goodenough, *Mater. Res. Bull.*, 1980, **15**, 783–789.
10 M. M. Thackeray, W. I. F. David, P. G. Bruce and J. B. Goodenough, *Mater. Res. Bull.*, 1983, **18**, 461–472.
11 M. S. Whittingham, *Science*, 1976, **192**, 1126–1127.
12 C. Masquelier and L. Croguennec, *Chem. Rev.*, 2013, **113**, 6552–6591.
13 D. Morgan, A. Van der Ven and G. Ceder, *Electrochem. Solid-State Lett.*, 2004, **7**, A30–A32.
14 K. Kang, Y. S. Meng, J. Breger, C. P. Grey and G. Ceder, *Science*, 2006, **311**, 977–980.
15 J.-M. Tarascon, E. Wang, F. K. Shokoohi, W. R. Mckinnon and S. Colson, *J. Electrochem. Soc.*, 1991, **138**, 2859–2864.
16 J. Lee, D.-H. Seo, M. Balasubramanian, N. Twu, X. Li and G. Ceder, *Energy Environ. Sci.*, 2015, **8**, 3255–3265.
17 J. C. Kim, D.-H. Seo, H. Chen and G. Ceder, *Adv. Energy Mater.*, 2015, **5**, 1401916.
18 D.-H. Seo, J. Lee, A. Urban, R. Malik, S. Kang and G. Ceder, *Nat. Chem.*, 2016, **8**, 692–697.
19 J. B. Goodenough and Y. Kim, *Chem. Mater.*, 2010, **22**, 587–603.
20 J. C. Kim, D.-H. Seo and G. Ceder, *Energy Environ. Sci.*, 2015, **8**, 1790–1798.
21 B. Kang and G. Ceder, *Nature*, 2009, **458**, 190–193.
22 M. Reynaud, M. Ati, B. C. Melot, M. T. Sougrati, G. Rousse, J.-N. N. Chotard and J.-M. Tarascon, *Electrochem. Commun.*, 2012, **21**, 77–80.
23 H. Chen, G. Hautier and G. Ceder, *J. Am. Chem. Soc.*, 2012, **134**, 19619–19627.
24 G. Rousse and J.-M. Tarascon, *Chem. Mater.*, 2014, **26**, 394–406.
25 M. Bianchini, F. Fauth, N. Brisset, E. Suard, C. Masquelier and L. Croguennec, *Chem. Mater.*, 2015, **27**, 3009–3020.
26 C. Delmas, C. Fouassier and P. Hagenmuller, *Physica B+C*, 1980, **99**, 81–85.
27 R. J. Clement, P. G. Bruce and C. P. Grey, *J. Electrochem. Soc.*, 2015, **162**, A2589–A2604.
28 M. Pollet, M. Blangero, J.-P. Doumerc, R. Decourt, D. Carlier, C. Denage and C. Delmas, *Inorg. Chem.*, 2009, **48**, 9671–9683.
29 Y. Mo, S. P. Ong and G. Ceder, *Chem. Mater.*, 2014, **26**, 5208–5214.
30 S. P. Ong, V. L. Chevrier, G. Hautier, A. Jain, C. J. Moore, S. Kim, X. Ma and G. Ceder, *Energy Environ. Sci.*, 2011, **4**, 3680–3688.
31 N. Yabuuchi, K. Kubota, M. Dahbi and S. Komaba, *Chem. Rev.*, 2014, **114**, 11636–11682.
32 L. Q. Zhang, K. Takada, N. Ohta, M. Osada and T. Sasaki, *J. Power Sources*, 2007, **174**, 1007–1011.
33 L. W. Shacklette, T. R. Jow and L. Townsend, *J. Electrochem. Soc.*, 1988, **135**, 2669–2674.
34 Y. Takeda, K. Nakahara, M. Nishijima, N. Imanishi, O. Yamamoto, M. Takano and R. Kanno, *Mater. Res. Bull.*, 1994, **29**, 659–666.
35 C. Didier, M. Guignard, C. Denage, O. Szajwaj, S. Ito, I. Saadoune, J. Darriet and C. Delmas, *Electrochem. Solid-State Lett.*, 2011, **14**, A75–A78.
36 X. Ma, H. Chen and G. Ceder, *J. Electrochem. Soc.*, 2011, **158**, A1307–A1312.
37 P. Vassilaras, X. Ma, X. Li and G. Ceder, *J. Electrochem. Soc.*, 2013, **160**, A207–A211.
38 C. Delmas, J. J. Braconnier, C. Fouassier and P. Hagenmuller, *Solid State Ionics*, 1981, **3–4**, 165–169.
39 J. J. Braconnier, C. Delmas and P. Hagenmuller, *Mater. Res. Bull.*, 1982, **17**, 993–1000.
40 A. Mendiboure, C. Delmas and P. Hagenmuller, *J. Solid State Chem.*, 1985, **57**, 323–331.
41 S. Komaba, N. Yabuuchi, T. Nakayama, A. Ogata, T. Ishikawa and I. Nakai, *Inorg. Chem.*, 2012, **51**, 6211–6220.
42 N. Yabuuchi, M. Kajiyama, J. Iwatate, H. Nishikawa, S. Hitomi, R. Okuyama, R. Usui, Y. Yamada and S. Komaba, *Nat. Mater.*, 2012, **11**, 512–517.
43 H. Yoshida, N. Yabuuchi and S. Komaba, *Electrochem. Commun.*, 2013, **34**, 60–63.
44 M. Sathiya, K. Hemalatha, K. Ramesha, J. M. Tarascon and A. S. Prakash, *Chem. Mater.*, 2012, **24**, 1846–1853.
45 D. Kim, E. Lee, M. Slater, W. Q. Lu, S. Rood and C. S. Johnson, *Electrochem. Commun.*, 2012, **18**, 66–69.
46 P. Vassilaras, A. J. Toumar and G. Ceder, *Electrochem. Commun.*, 2014, **38**, 79–81.
47 X. Li, D. Wu, Y. N. Zhou, L. Liu, X. Q. Yang and G. Ceder, *Electrochem. Commun.*, 2014, **49**, 51–54.
48 C. Delmas, I. Saadoune and P. Dordor, *Mol. Cryst. Liq. Cryst. Sci. Technol., Sect. A*, 1994, **244**, 337–342.
49 L. Demourguesguerlou, J. J. Braconnier and C. Delmas, *J. Solid State Chem.*, 1993, **104**, 359–367.
50 G. Kresse and J. Furthmuller, *Phys. Rev. B: Condens. Matter Mater. Phys.*, 1996, **54**, 11169–11186.
51 P. E. Blochl, *Phys. Rev. B: Condens. Matter Mater. Phys.*, 1994, **50**, 17953–17979.
52 J. P. Perdew, K. Burke and M. Ernzerhof, *Phys. Rev. Lett.*, 1996, **77**, 3865–3868.
53 V. L. Chevrier, S. P. Ong, R. Armiento, M. K. Y. Chan and G. Ceder, *Phys. Rev. B: Condens. Matter Mater. Phys.*, 2010, **82**, 075122.
54 J. Heyd, G. E. Scuseria and M. Ernzerhof, *J. Chem. Phys.*, 2003, **118**, 8207–8215.
55 J. Heyd, G. E. Scuseria and M. Ernzerhof, *J. Chem. Phys.*, 2006, **124**, 219906.
56 A. Jain, G. Hautier, S. P. Ong, C. J. Moore, C. C. Fischer, K. A. Persson and G. Ceder, *Phys. Rev. B: Condens. Matter Mater. Phys.*, 2011, **84**, 045115.
57 A. Jain, G. Hautier, C. J. Moore, S. P. Ong, C. C. Fischer, T. Mueller, K. A. Persson and G. Ceder, *Comput. Mater. Sci.*, 2011, **50**, 2295–2310.
58 S. P. Ong, W. D. Richards, A. Jain, G. Hautier, M. Kocher, S. Cholia, D. Gunter, V. L. Chevrier, K. A. Persson and G. Ceder, *Comput. Mater. Sci.*, 2013, **68**, 314–319.
59 I. Saadoune, A. Maazaz, M. Menetrier and C. Delmas, *J. Solid State Chem.*, 1996, **122**, 111–117.

60 X. F. Wang, G. D. Liu, T. Iwao, M. Okubo and A. Yamada, *J. Phys. Chem. C*, 2014, **118**, 2970–2976.
61 R. Fielden and M. N. Obrovac, *J. Electrochem. Soc.*, 2015, **162**, A453–A459.
62 X. Li, X. Ma, D. Su, L. Liu, R. Chisnell, S. P. Ong, H. Chen, A. Toumar, J. C. Idrobo, Y. C. Lei, J. M. Bai, F. Wang, J. W. Lynn, Y. S. Lee and G. Ceder, *Nat. Mater.*, 2014, **13**, 586–592.
63 N. Meethong, H. Y. S. Huang, S. A. Speakman, W. C. Carter and Y. M. Chiang, *Adv. Funct. Mater.*, 2007, **17**, 1115–1123.
64 S. Kim, X. H. Ma, S. P. Ong and G. Ceder, *Phys. Chem. Chem. Phys.*, 2012, **14**, 15571–15578.
65 J. Ma, S. H. Bo, L. Wu, Y. Zhu, C. P. Grey and P. G. Khalifah, *Chem. Mater.*, 2015, **27**, 2387–2399.
66 S. H. Bo, X. Li, A. J. Toumar and G. Ceder, *Chem. Mater.*, 2016, **28**, 1419–1429.
67 A. Jain, S. P. Ong, G. Hautier, W. Chen, W. D. Richards, S. Dacek, S. Cholia, D. Gunter, D. Skinner, G. Ceder and K. A. Persson, *APL Mater.*, 2013, **1**, 011002.
68 B. J. Hwang, Y. W. Tsai, D. Carlier and G. Ceder, *Chem. Mater.*, 2003, **15**, 3676–3682.
69 L. Wang, T. Maxisch and G. Ceder, *Phys. Rev. B: Condens. Matter Mater. Phys.*, 2006, **73**, 195107.
70 H. Gwon, D.-H. Seo, S. W. Kim, J. Kim and K. Kang, *Adv. Funct. Mater.*, 2009, **19**, 3285–3292.
71 G. Ceder, Y. M. Chiang, D. R. Sadoway, M. K. Aydinol, Y. I. Jang and B. Huang, *Nature*, 1998, **392**, 694–696.
72 J. Graetz, C. Ahn, H. Ouyang, P. Rez and B. Fultz, *Phys. Rev. B: Condens. Matter Mater. Phys.*, 2004, **69**, 235103.
73 H. Tan, J. Verbeeck, A. Abakumov and G. Van Tendeloo, *Ultramicroscopy*, 2012, **116**, 24–33.
74 I. Saadoune and C. Delmas, *J. Solid State Chem.*, 1998, **136**, 8–15.
75 C. Delmas, G. Prado, A. Rougier, E. Suard and L. Fournes, *Solid State Ionics*, 2000, **135**, 71–79.
76 D. P. Abraham, R. D. Twesten, M. Balasubramanian, J. Kropf, D. Fischer, J. McBreen, I. Petrov and K. Amine, *J. Electrochem. Soc.*, 2003, **150**, A1450–A1456.
77 A. Rougier, C. Delmas and A. V. Chadwick, *Solid State Commun.*, 1995, **94**, 123–127.
78 M. Balasubramanian, X. Sun, X. Q. Yang and J. McBreen, *J. Electrochem. Soc.*, 2000, **147**, 2903–2909.
79 C. S. Johnson and A. J. Kropf, *Electrochim. Acta*, 2002, **47**, 3187–3194.
80 L. A. Montoro, M. Abbate and J. M. Rosolen, *J. Electrochem. Soc.*, 2000, **147**, 1651–1657.
81 Y. Nanba, T. Iwao, B. Mortemard de Boisse, W. Zhao, E. Hosono, D. Asakura, H. Niwa, H. Kiuchi, J. Miyawaki, Y. Harada, M. Okubo and A. Yamada, *Chem. Mater.*, 2016, **28**, 1058–1065.
82 A. J. Toumar, S. P. Ong, W. D. Richards, S. Dacek and G. Ceder, *Phys. Rev. Appl.*, 2015, **4**, 064002.
83 H. Xia, L. Lu, Y. S. Meng and G. Ceder, *J. Electrochem. Soc.*, 2007, **154**, A337–A342.
84 C. Delmas, M. Menetrier, L. Croguennec, I. Saadoune, A. Rougier, C. Pouillerie, G. Prado, M. Grune and L. Fournes, *Electrochim. Acta*, 1999, **45**, 243–253.
85 J. C. Kim, X. Li, C. J. Moore, S. H. Bo, P. G. Khalifah, C. P. Grey and G. Ceder, *Chem. Mater.*, 2014, **26**, 4200–4206.
86 N. Yabuuchi, H. Yoshida and S. Komaba, *Electrochemistry*, 2012, **80**, 716–719.
87 L. Liu, X. Li, S. H. Bo, Y. Wang, H. Chen, N. Twu, D. Wu and G. Ceder, *Adv. Energy Mater.*, 2015, **5**, 1500944.
88 J. S. Thorne, S. Chowdhury, R. A. Dunlap and M. N. Obrovac, *J. Electrochem. Soc.*, 2014, **161**, A1801–A1805.
89 X. Li, Y. Wang, D. Wu, L. Liu, S. H. Bo and G. Ceder, *Chem. Mater.*, 2016, **28**, 6575–6583.